Relating Structural Aspects of Bimetallic Pt₃Cr₁/C Nanoparticles to Their Electrocatalytic Activity, Stability, and Selectivity in the Oxygen Reduction Reaction

Fadlilatul Taufany,[a] Chun-Jern Pan,[a] Hung-Lung Chou,[a] John Rick,[a] Yong-Siou Chen,[a] Din-Goa Liu,[b] Jyh-Fu Lee,[b] Mau-Tsu Tang,[b] and Bing-Joe Hwang *[a, b]

Abstract: Two methods were used to prepare bimetallic Pt₃Cr₁/C nanocatalysts with similar composition but different alloying extent (structure). We investigated how these differences in alloying extent affect the catalytic activity, stability and selectivity in the oxygen reduction reaction (ORR). One method, based on slow thermal decomposition of the Cr precursor at a rate that matches that of chemical reduction of the Pt precursor, allows fine control of the composition of the Pt₃Cr₁/C alloy, whereas the second approach, using the ethylene glycol method, results in considerable deviation (>25%) from the projected composition. Consequently, these two methods lead to variations in the alloying extent that strongly influence the Pt d-band vacancy and the Pt electroactive surface area (Pt ESCA). This relationship was systematically evaluated by transmission electron microscopy, X-ray absorption near edge structure spectroscopy, and electrochemical analysis. The ORR activity depends on two effects that nullify each other, namely, the number of active Pt sites and their activity. The Pt-site activity is more dominant in governing the ORR activity. The selectivity of the nanocatalyst towards the ORR and the competitive methanol oxidation reaction (MOR) depend on these two effects acting in cooperation to give enhanced ORR activity with suppressed MOR. The number of active Pt sites is associated with the Pt ESCA value, while Pt-site activity is associated with the alloying extent and Pt d-band vacancy (electronic) effects. The presence of Cr atoms in Pt₃Cr₁/C enhances stability during electrochemical treatment. Overall, the Pt₃Cr₁/C catalyst prepared by controlled-composition synthesis was shown to be superior in ORR activity, selectivity and stability owing to its favorable alloying extent, Pt d-band vacancy, and Pt ESCA.

Keywords: alloys · chromium · electrochemistry · nanoparticles · platinum

Introduction

The composition of bimetallic nanoparticles (NPs) must be rigorously controlled during the fabrication process, as their alloy composition is fundamental to their potential as highly efficient catalysts,[1,2] independent magnetic components for ultrahigh-density memory devices,[3,4] and sensors in the biomedical field.[5] Efforts to understand the physical chemistry behind bimetallic NP composition have been paralleled by attempts to exploit their beneficial properties for these applications. In most cases composition plays a significant role in determining the alloying extent or atomic distribution between two different metals, which has a significant influence on NP activity,[6,7] coercivity,[8,9] stability,[10] and selectivity.[11] Techniques such as transmission electron microscopy (TEM) coupled to energy dispersive X-ray analysis (EDX) make it possible to obtain reasonably good estimates of the alloy composition in bimetallic NPs. X-ray absorption spectroscopy (XAS) is a powerful technique for investigating the internal structure of the bulk and surface regions of NPs.[12] The two techniques, in combination, provide mechanistic insight into the atomistic bulk/surface chemistry of the NPs governing their enhanced properties.

Among bimetallic systems, Pt–M alloy NPs in which M is a 3d transition metal, such as Cr, Mn, Fe, Co, or Ni, have received renewed interest from both the scientific and industrial communities, due to their multifunctionality and enhanced properties that can be broadly exploited for the above applications.[7–9] However, the rationale underpinning their design is an on-going challenge. Generally, the main problems regarding the preparation of carbon-supported Pt–M (Pt–M/C) alloy NPs are the poor content of 3d transition

[a] Dr. F. Taufany, Dr. C.-J. Pan, Dr. H.-L. Chou, Dr. J. Rick, Y.-S. Chen, Prof. B.-J. Hwang
Department of Chemical Engineering
National Taiwan University of Science and Technology
#43, Sec.4, Keelung Rd., Taipei, 10607, Taiwan (R.O.C.)
E-mail: bjh@mail.ntust.edu.tw

[b] D.-G. Liu, Dr. J.-F. Lee, Dr. M.-T. Tang, Prof. B.-J. Hwang
National Synchrotron Radiation Research Center
101 Hsin-Ann Road, Hsinchu Science Park, Hsinchu 30076, Taiwan (R.O.C)

Supporting information for this article is available on the WWW under http://dx.doi.org/10.1002/chem.201100556.

metals in the alloy and the increase in particle size with respect to pure Pt.[13] The former problem occurs because the true alloy composition involving the 3d transition metal, which is difficult to reduce during synthesis, remains below the designed composition.

A common method used to prepare carbon-supported Pt–M alloy NPs is deposition of the 3d transition metals on previously formed carbon-supported platinum (Pt/C), followed by alloying at high temperatures. This thermal treatment at high temperatures ($\geq 900\,°C$) gives rise to undesired metal-particle growth by sintering and coalescence of Pt particles.[14] By using a lower reaction temperature ($\leq 200\,°C$) with colloidal methods such as sodium borohydride reduction, sulfite-complex reduction, or the polyalcohol (or polyol) reduction process, sintering of the alloy particles is significantly suppressed, but the control of alloy composition remains difficult.[15] This is attributed to a large difference in the driving force for the reduction process with respect to the Pt and M precursors; that is, Pt has a higher redox potential and is preferentially reduced first, whereas the M precursor still struggles to fully attain the metallic state, since this process only uses low temperature conditions and relatively weak reducing agents for the M precursors. Recently, using organometallic precursors, Sun et al.[8,9] succeeded in preparing monodisperse Pt–Fe alloy NPs by simultaneous reduction of [Pt(acac)$_2$] and [Fe(acac)$_2$] (acac = acetylacetonate) in reverse micelles. These metal–organic precursors are easily decomposed by thermal treatment to form the metallic state, and the reduction process is altered in such a way that the driving forces for reduction of the Pt and M precursors become similar. This, together with the presence of reverse micelles as nanocapsules, that is, a kind of limited reaction space, can provide monodisperse alloy particles with uniform composition. Liu et al.[16] examined the applicability of this method to deposition of Pt–Ru NPs on carbon-black supports, whereby the alloy NPs were first precipitated by removing the organic moieties (i.e., the capsules), followed by addition of carbon supports. However, without any protection by the organic moieties, these naked alloy NPs were found to be partially aggregated on the supports. Thus, it is still challenging to prepare highly dispersed alloy NPs by such a "post-supporting" method.

By re-examining the challenges in previous strategies, we aim to report controlled composition-based synthesis and characterization of selected carbon-supported bimetallic NPs and simultaneously demonstrate their unique properties, that is, the alloying extent, by focusing on catalytic activity, stability, and selectivity, using a oxygen reduction reaction (ORR) as a model system; ORR is a key reaction for the practical implementation of direct methanol fuel cells (DMFCs). Pt–Cr/C NPs were chosen as primary example because Mukerjee et al.[17] found that the ORR activity of these Pt–M/C alloys follows a volcano-type profile with respect to both of their structural (Pt–Pt distance) and electronic (Pt d-band vacancy) properties, and Pt–Cr/C showed the highest activity. These NPs can potentially address the principal drawbacks in the ORR, namely, the sluggish kinet-

ics and high Pt loadings. The Pt–Cr alloy has also been characterized as a stable catalyst in acidic[18] and oxidizing media at high temperatures under fuel-cell operating conditions.[19] The selectivity towards the ORR, in particular for these Pt-Cr alloy NPs, has been recently tested by Lamy et al.[20] In general, the selectivity is principally associated with methanol crossover from anode to cathode side, that is, passage through the DMFC membrane. This is potentially a site at which the ORR performance may be reduced due to occurrence of a mixed potential resulting from competitive reactions, such as oxygen reduction and methanol oxidation. Their results showed that the Pt–Cr alloy is a selective and active catalyst that can catalyze oxygen reduction with suppressed oxidation of methanol.

Despite significant progress in the development of Pt–Cr/C catalysts, the structural (alloying extent) effect originating from controlled composition-based synthesis on their ORR activity, stability, and selectivity, has not been simultaneously studied so far. To obtain monodisperse Pt$_3$Cr$_1$/C alloy NPs, while retaining precise control over their alloy composition, we developed a synthetic strategy in which reduction of the [Pt(acac)$_2$] precursor by a polyol, for example, ethylene glycol, is instead performed with long-chain 1,2-hexadecanediol to produce Pt^0 particles at $120\,°C$, and the [Cr(acac)$_3$] precursor is replaced by a low-boiling organometallic species, namely, [Cr(CO)$_6$], to form Cr^0 particles by slow thermal decomposition at $290\,°C$, ensuring that the driving forces for reduction of the Pt and Cr precursors are similar. Both chemical reactions were initiated together in the presence of oleic acid and oleylamine, that is, in a nanocapsule reaction space that provides a convenient route for stabilizing the monodisperse alloy NPs and prevents their being oxidized. Starting from the same projected alloy composition, Pt$_3$Cr$_1$/C NPs were also prepared by the polyol method, using ethylene glycol (EG) as reducing agent,[21] whereby the driving forces for reduction of the Pt and Cr precursors are significantly different. As a result, these two methods lead to different bimetallic alloy compositions and affect the most essential physiochemical property of the Pt$_3$Cr$_1$/C NPs, that is, the alloying extent, which has a strong influence on the other physiochemical properties, such as the Pt d-band vacancy and Pt-electroactive surface area (Pt ESCA). Transmission electron microscopy (TEM), X-ray absorption near edge structure (XANES), electrochemical, and the first-principles density functional theory (DFT) calculations were employed to determine the above-mentioned physiochemical properties. Here, we describe how variations in the alloying extent of bimetallic Pt$_3$Cr$_1$/C NPs influence their catalytic activity, stability and selectivity with respect to the ORR.

Results and Discussion

Scheme 1 illustrates the preparation protocol of the monodisperse Pt$_3$Cr$_1$/C alloy NPs, in which tight control over alloy composition is maintained by using a combination of chemi-
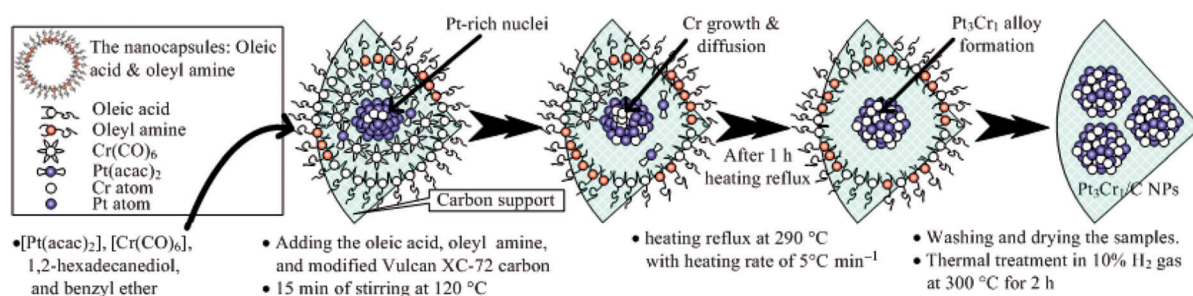
Scheme 1. The preparation procedure for the Pt_3Cr_1/C NPs by combined chemical reduction and thermal decomposition of Pt and Cr precursors (TD method).

cal reduction and thermal decomposition (TD). In the early stage of the synthesis, at 120 °C, Pt-rich nuclei are formed by chemical reduction of $[Pt(acac)_2]$ and the slow decomposition of the volatile organometallic precursor $[Cr(CO)_6]$ in the presence of oleylamine and oleic acid as stabilizers. Heating the reaction mixture to reflux at 290 °C (initial heating rate 5 °C min^{-1}) leads, after approximately 1 h, to growth and subsequent diffusion of Cr atoms into the previously formed Pt-rich nuclei with complete decomposition of $[Cr(CO)_6]$. The $[Cr(CO)_6]$ precursor has a boiling point of 210 °C, and is in the vapour phase at the reaction temperature of 290 °C. Formation of this vapour phase results from slow decomposition of $[Cr(CO)_6]$ at a rate that matches the reduction rate of $[Pt(acac)_2]$, and this is the key point of the present composition-controlled synthesis. A high-boiling solvent with chemical stability at such a high temperature, for example, benzyl ether, is consequently required in this strategy to provide a medium for complete nucleation, growth and interatomic diffusion of the particles. Therefore, the present strategy takes into account all the important aspects regarding the uniform-size and composition-controlled synthesis of bimetallic NPs, that is, stabilizer, solvent, reducing agent, and reaction temperature.

For comparison, NPs with the same Pt_3Cr_1/C composition were prepared by the EG method, in which electrons generated on oxidation of EG to glycolic acid or glycolate anion (depending on pH) are used to reduce the Pt and Cr precursors at 160 °C, while the resulting EG derivatives act as a stabilizing agent for the PtCr colloids and thus lead to well-dispersed bimetallic PtCr/C NPs.[21] However, under such mild temperature conditions, the reduction of 3d transition metal compounds such as $CrCl_3$ occurs at a lower rate than that of $PtCl_4$, and this results in a large deviation in the designed Pt–Cr composition. However, this method can not be carried out a higher temperature due to the instability of EG at high temperature. Hence, the two presented methods give different alloy compositions of Pt_3Cr_1/C NPs leading to variations in their physiochemical properties.

Transmission electron micrographs of Pt_3Cr_1/C NPs prepared by the TD and the conventional EG methods are shown in Figure 1a and d, respectively. Both types of Pt_3Cr_1/C NPs were found to be uniformly dispersed on their carbon supports with reasonably narrow size distributions of about 3–3.5 nm. In the present TD method, such an excel-

lent control over particle size and dispersion was obtained principally due to the presence of oleic acid and oleylamine in the metal precursor solution, which act as a stabilizing agent[5,7–11] that can generate nanocapsules as reaction space. Because the particles were formed by chemical reduction and decomposition of metal precursors in these nanocapsules, they exhibited uniform dimensions within a narrow size distribution. The adsorbed organic nanocapsules on the surface of the NPs also create repulsion between them, and hence well-dispersed NPs. Both oleic acid and oleylamine are known for their good ligand capability towards metal atoms, since their tails at the double bond of the hydrocarbon chains are kinked, which is critical to their effectiveness; stearic acid, for example, does not stabilize colloidal precursors. Oleic acid has been used to stabilize variety of colloids including Cr NPs.[22] Similarly, oleylamine is good stabilizing ligand for noble metals such as Pt.[8,9,23–25]

Based on the EDX spectra (Figure 1b and e), the alloy composition of both types of Pt_3Cr_1/C NPs was quantitatively analyzed, and the results are summarized in Table 1. The

Table 1. Physiochemical properties of Pt_3Cr_1/C NPs.

| | Composition [atom%] | | a_{av}[a] | AE[b] | h_{Ts}[c] | Pt ESCA |
	Pt	Cr	[Å]	[%]		[m^2 g^{-1}]
Pt_3Cr_1/C TD	73.78	26.22	3.888	54	1.4687	43.44
Pt_3Cr_1/C EG	84.57	15.43	3.903	24	1.5199	62.96

[a] Lattice parameter. [b] Alloying extent. [c] Pt d-band vacancy.

Pt_3Cr_1/C NPs prepared by the present TD method have an average alloy composition of $Pt_{74}Cr_{26}$ with only a slight deviation of 3.25 atom% from the designed composition of $Pt_{75}Cr_{25}$. Thus, the composition of the Pt_3Cr_1/C TD NPs is well controlled. In contrast, the catalyst prepared by the conventional EG method has an average alloy composition of $Pt_{85}Cr_{15}$ with a deviation of more than 25% compared to the designed composition, due to the difficulty of reducing the Cr precursor.[22] From the difference in the resulting alloy composition of both Pt_3Cr_1/C NPs, the two NPs should have different physiochemical properties (e.g., alloying extent, Pt d-band vacancy, Pt electroactive surface area).

Figure 1c and f display the ring diffraction patterns for Pt_3Cr_1/C NPs prepared by the TD and EG methods, respectively. A larger grain size of the particles usually gives a
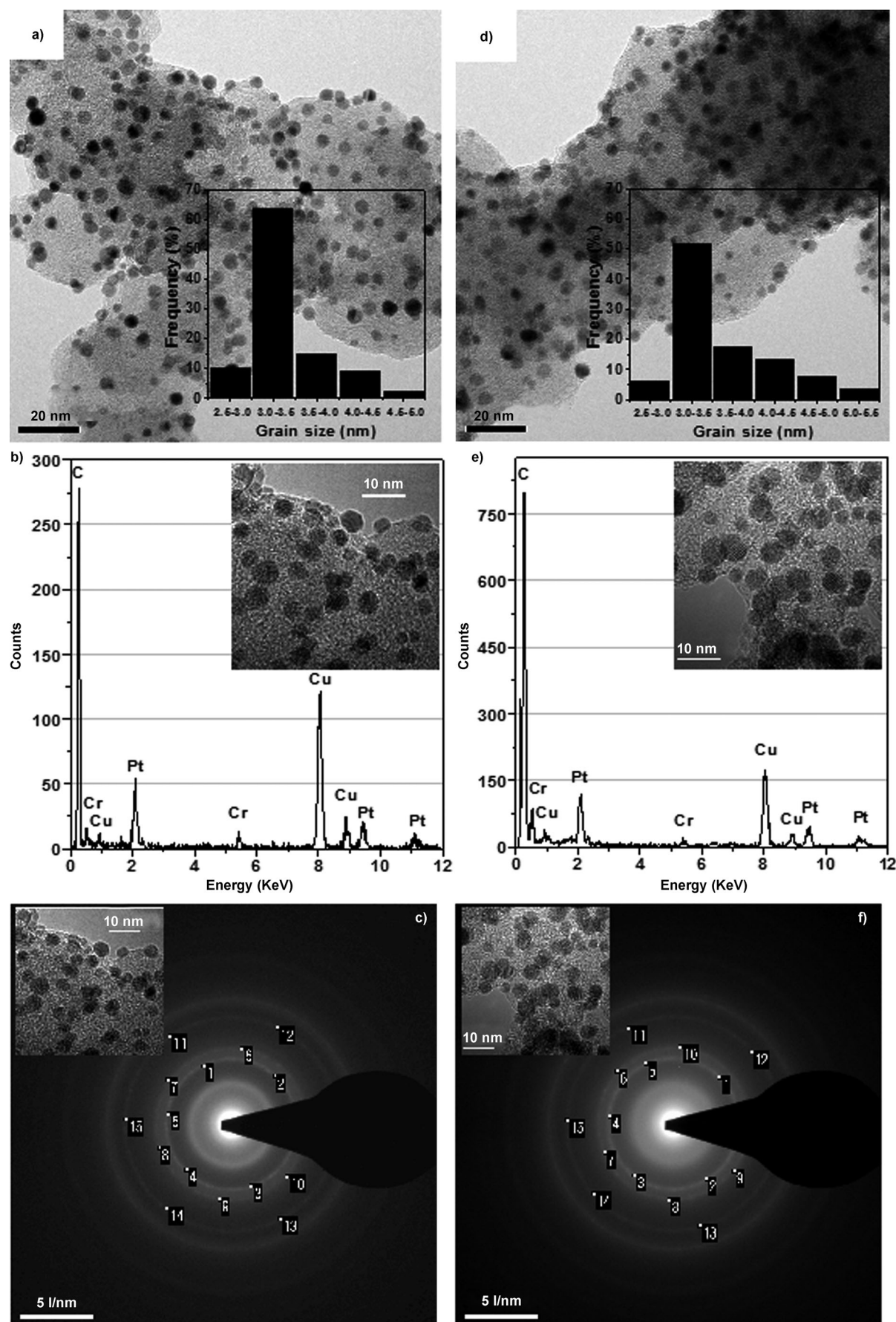
Figure 1. a) TEM images, b) EDX spectrum, and c) ring-diffraction pattern of Pt$_3$Cr$_1$/C NPs prepared by TD method in comparison with those of reference NPs prepared by the EG method (d–f). The HRTEM images used for data extraction are given in the insets.

bright speckled pattern, and a finer grain size gives a continuous ring pattern.[26] Both types of Pt_3Cr_1/C NPs show a continuous bright ring, indicating their nanosize. A series of ring patterns with different radii in both NPs are due to the presence of polycrystals with different planes. Pure platinum has an fcc structure, and pure chromium a bcc structure. However, for both types of Pt_3Cr_1/C NPs diffraction from the Pt fcc lattice structure alone could be observed. This can be attributed to formation of bimetallic Pt–Cr alloy with a single-phase solid solution.[18,20,27]

Spot analysis of the ring pattern TEM (Supporting Information, Table S1) confirms formation of disordered Pt fcc structure with (111), (200), (220), (311), and (222) planes on both types of Pt_3Cr_1/C NPs. The average lattice parameter a_{av} of the solid solution was quantified by considering the (111), (200), and (220) planes. It is noteworthy that the lattice parameters of both the Pt_3Cr_1/C TD ($a_{av} = 3.888$ Å) and Pt_3Cr_1/C EG ($a_{av} = 3.903$ Å) NPs are smaller than that of Pt/C NPs ($a_{av} = 3.919$ Å). The lattice contraction after alloying of Pt with Cr clearly indicates conversion of Cr atoms to an alloyed state to form a solid solution of PtCr, as expected from the Vegard's law (linear relationship between lattice parameter and alloy composition).[28]

Recently, Gonzalez et al.[29] used the lattice parameter to evaluate the alloying extent between two constituent elements in bimetallic Pt-based alloys. The alloying extent (AE) in the supported Pt–Cr catalysts is calculated by using Equation (1)

$$AE = \frac{a_{av} - a_0}{a_c - a_0} \times 100\%$$ (1)

where a_0 is the lattice parameter of carbon-supported platinum (Pt/C), and a_c the lattice parameter under the assumption that all chromium is alloyed. The alloying extent of Pt_3Cr_1/C TD NPs is approximately 2.25 times higher than that of the Pt_3Cr_1/C EG NPs (Table 1). This could be explained by the fact that the method based on combined chemical reduction of the Pt precursor and thermal decomposition of the $[Cr(CO)_6]$ precursor can provide better control over the Pt–Cr alloy composition than the conventional EG-based method, which still suffers from difficulty in reducing the Cr precursor. The higher Cr content in the Pt_3Cr_1/C TD NPs tends to enhance the heteroatomic interactions and allows incorporation of more Cr atoms into the fcc lattice of Pt, resulting in a decreased lattice parameter and subsequent increase in alloying extent, in accordance with Vegard's law.

To gain more insight into the bulk properties of the Pt_3Cr_1/C NPs (i.e., Pt electronic properties such as d-band vacancy), XANES was employed. In our previous studies, X-ray absorption spectroscopy (XAS), encompassing both XANES and extended X-ray absorption fine structure (EXAFS), has proved to be a powerful structural-characterization technique for investigating oxidation states, d-band vacancies, and the environment surrounding an absorbing atom.[6,13,30–34] The raw background-subtracted k^2-weighted

Pt L_3-edge EXAFS data ($\Delta k = 2.0$–16.0 Å^{-1}) collected for both the Pt_3Cr_1/C NPs and a Pt reference foil (Supporting Information, Figure S1) show a high signal-to-noise ratio and allow the EXAFS oscillations to be clearly observed, and thus indicate good data quality for both the XANES and the EXAFS spectra (Supporting Information, Figure S2) discussed here.

Figure 2 shows the Pt L_3-edge XANES spectra for the Pt_3Cr_1/C alloy NPs and for the Pt foil. The absorption at 11 564 eV corresponds to a $2p_{3/2} \rightarrow 5d$ electronic transition,
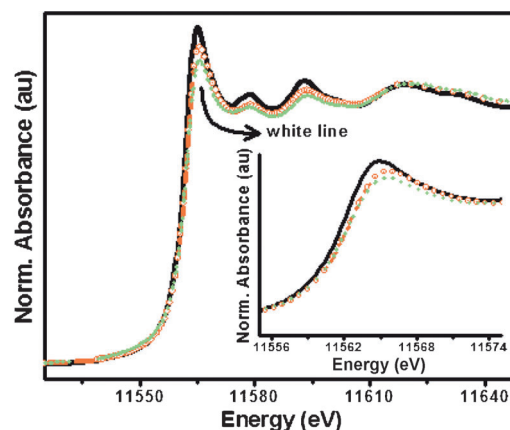

Figure 2. Pt L_3-edge XANES spectra for Pt_3Cr_1/C EG (orange line) and Pt_3Cr_1/C TD (green line) NPs and the Pt reference foil (black line).

which results, at the threshold, in a sharp peak known as the white line, the integrated intensity of which is related to the 5d electron vacancies; the lower the intensity the lower is the 5d band vacancy and vice versa.[35] The white-line intensities for both types of Pt_3Cr_1/C NPs are lower than that of Pt foil. This could be due to alloying of Cr with Pt leading to a high electron density around Pt atoms. This phenomenon causes a decrease in the Pt d-band vacancy, and in turn a decrease in the white line was observed for the Pt_3Cr_1/C NPs.

To quantify the difference in white-line intensity between the Pt_3Cr_1/C NPs and the Pt foil, a method modified by Reifsnyder et al.,[36] which was originally developed by Mansour et al.,[35] was adopted in this study. After subtracting the platinum-foil data from the catalyst data, the resulting curves were numerically integrated between -10 and $+14$ eV for both the L_2 (ΔA_2) and L_3 (ΔA_3) edges. The fractional change in total number of d-band vacancies of the sample, compared to the number in the platinum foil f_d was calculated by using Equation (2).

$$f_d = \frac{\Delta A_3 \sigma_3 + 1.11 \Delta A_2 \sigma_2}{\Delta A_{3r} \sigma_3 + 1.11 \Delta A_{2r} \sigma_2}$$ (2)

The areas are normalized by multiplying by the X-ray absorption cross section at the edge jump σ. Values of 117.1 and 54.2 cm^{2}g^{-1} were used for the absorption cross section at the platinum L_3- and L_2-edges, respectively.[37] When the

d-band vacancy in the reference material h_{Tr} is known,[38] the d-band vacancy of the sample h_{Ts} can be calculated by using Equation (3).

$$h_{Ts} = (1 + f_d)h_{Tr} \qquad (3)$$

The Pt d-band vacancies h_{Ts} for both types of Pt$_3$Cr$_1$/C NPs are lower than that of Pt foil (Figure 3). This strongly
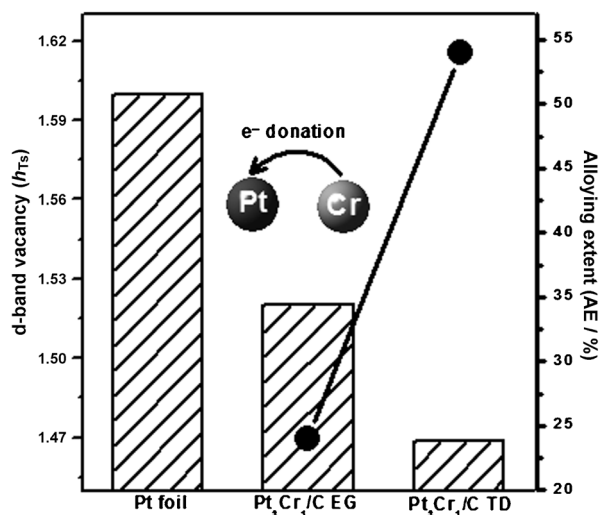

Figure 3. Relationship between d-band vacancy (hashed bars) and alloying extent (black line) for the Pt$_3$Cr$_1$/C NPs prepared by the TD and EG methods.

supports the idea that the 5d electron density around the Pt atoms in the Pt$_3$Cr$_1$/C NPs increases due to partial electron donation from Cr to Pt atoms as a result of the hybridization between Cr (3d) and Pt (5d) states. Additionally, the h_{Ts} value of the d-band vacancy decreases with increasing alloying extent, as observed in the case of Pt$_3$Cr$_1$/C TD NPs. Since the Pt$_3$Cr$_1$/C NPs are formed in a more controlled manner, their composition is closer to that theoretically calculated, that is, more Cr atoms were alloyed with Pt, thereby increasing the extent of hybridization of Cr (3d) and Pt (5d) states, while more electrons were transferred from Cr to Pt; this eventually generates fewer d-band vacancies. This partial electron-donation effect from the Cr to Pt atoms is also in a good agreement with the results from our first-principles DFT modeling-based study (Supporting Information, Figure S3 and Table S2). Moreover, from this DFT modeling, the value of the d-band center was found to be shifted from -2.21 eV in pure Pt to -2.65 eV in Pt$_3$Cr$_1$ system (Supporting Information, Table S2). This finding is consistent with a study by Nørskov et al.,[39] whereby the d-band center of Pt$_3$M$_1$ alloys (M is a 3d transition metals) was found to be higher than that of Pt.

Cyclic voltammetry (CV) can provide some information about the surface state of metal NPs. Figure S4 (Supporting Information) compares the voltammograms of Pt$_3$Cr$_1$/C catalysts prepared by TD and EG methods. Their anodic currents in the hydrogen region (0–0.33 V) corresponding to

oxidation of the hydrogen adatoms on Pt are clearly different, and thus indicate a difference in their Pt electroactive surface area (Pt ESCA). Combining the coulombic charge ($Q_{H\text{-des}}$) obtained from the hydrogen desorption peak and the amount of Pt used within the catalyst layer w_{Pt}, Pozio et al.[40] calculated the Pt ESCA by means of Equation (4)

$$\text{Pt ESCA} \left[\text{m}^2 \text{ g}^{-1}\right] = \frac{(Q_{H\text{-des}} [\text{C}]) \times 100}{210 \text{ }\mu\text{C cm}^{-2} \cdot (w_{Pt} [\text{g}])} \qquad (4)$$

where 210 μC cm^{-2} is the charge required to oxidize a monolayer of adsorbed hydrogen on Pt.[41,42] The calculated Pt ESCA for the Pt$_3$Cr$_1$/C TD catalyst is about 19.52 m^{2}g^{-1} lower than that of Pt$_3$Cr$_1$/C EG reference catalyst (Table 1), that is, this catalyst has a greater surface population of Cr atoms relatively to the reference catalyst as a result of its ability to provide more Cr metallic states close to the designed composition. From Figure S4 of the Supporting Information, it is also evident that the onset of oxide formation and the peak potential of oxide reduction for the Pt$_3$Cr$_1$/C TD catalyst are shifted to more positive potentials compared to those of the reference catalyst, that is, the alloying of Pt with a higher Cr content more strongly induces changes in the Pt electronic structure, and consequently inhibits the chemisorption of oxygenated species such as OH on the Pt sites at high potentials (>0.8 V). This may have a beneficial effect on oxygen adsorption at low overpotentials, which could lead to enhanced ORR kinetics.[18]

Linear scan voltammetry (LSV) was used to evaluate ORR kinetics on both Pt$_3$Cr$_1$/C TD and Pt$_3$Cr$_1$/C EG catalysts (Figure 4a). For all the catalysts, the ORR is diffusion-controlled when the potential is less than 0.7 V, and under mixed control from 0.7 to 0.85 V. In the mixed-control and kinetic regions (>0.85 V), the ORR activities for all the catalysts show a significant difference in magnitudes. It can be clearly seen from the Figure that the Pt$_3$Cr$_1$/C TD and Pt$_3$Cr$_1$/C EG catalysts show a drastically enhanced activity in a portion of the curves compared to commercial Pt/C E-tek. This Pt/C catalyst has a particle size in the range of 3 to 3.5 nm (see TEM image in Supporting Information, Figure S5) with an average particle size of 3.2 nm, which is comparable with those of both Pt$_3$Cr$_1$/C catalysts investigated here. Moreover, the Pt$_3$Cr$_1$/C TD catalyst has a higher activity towards the ORR than the Pt$_3$Cr$_1$/C EG catalyst. This is reflected in the mass activity, which represents the applicability of the catalyst in the ORR. The value of 26.10 A g$_{Pt}^{-1}$ at 0.9 V for the Pt$_3$Cr$_1$/C TD catalyst is more than three times that of Pt$_3$Cr$_1$/C EG (6.99 A g$_{Pt}^{-1}$) and nearly six times that of Pt/C (4.32 A g$_{Pt}^{-1}$), as shown in Figure 4b. To calculate the mass activity i_m of the catalysts, first the mass transport correction for the RDE was evaluated [Eq. (5)]

$$i_k = \frac{i_d \cdot i}{i_d - i} \qquad (5)$$

where i is the experimentally obtained current, i_d the measured diffusion-limited current, and i_k the mass-transport

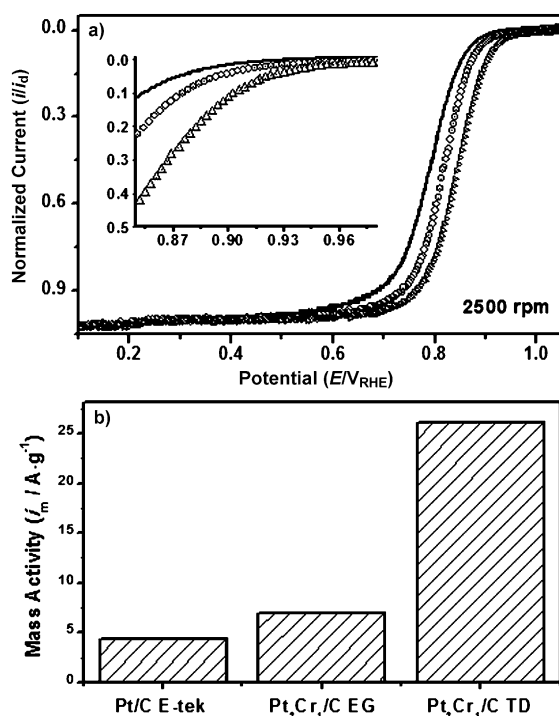Figure 4. a) Linear-scan voltammograms (LSVs) recorded at $1\,mV\,s^{-1}$ for the ORR on Pt/C E-tek (black line, 20 wt%) and the Pt_3Cr_1/C EG (circles) and Pt_3Cr_1/C TD (triangles) catalysts with rotation rate of 2500 rpm in O_2-saturated $0.5\,M\,H_2SO_4$ at 25°C. Inset: Magnified region of high positive potential. b) Corresponding mass activities measured at 0.90 V; bars indicate i_m at 0.9 V.

free kinetic current.[13] The mass activity i_m was then obtained via calculation of i_k [Eq. (5)] and normalized with the weight of Pt used [Eq. (6)].

$$i_m = \left(\frac{i_k\,[A]}{w_{Pt}\,[g]}\right)_{0.9\,V_{RHE}} \tag{6}$$

The activity of catalysts in heterogeneous reactions is generally dependent on at least two intimately linked parameters: 1) the number of available surface sites per unit mass and 2) the activity of each such site. The number of surface sites per unit mass in the context of bimetallic NPs is proportional to the surface population of the active sites, that is, the Pt electroactive site utilized in the ORR of the present case, and it can also be drastically increased by use of small NPs as long as the size is greater than the minimum dimension required to catalyze a specific reaction. In this case, the size effect on the ORR[43–45] is minimized as both the Pt_3Cr_1/C catalysts have similar particle size of approximately 3–3.5 nm, and thus it can be excluded from the discussion. The activity of a catalytic site is generally determined by its structural and electronic properties for a specific reaction to be catalyzed, where in this case the structural and electronic properties of the Pt_3Cr_1/C catalyst could be correlated to their alloying extents and Pt d-band vacancy, respectively.

Interestingly, the lower Pt electroactive surface areas in Pt_3Cr_1/C TD catalyst show higher ORR mass activity. This seems contradictory because a smaller Pt electroactive surface would tend to decrease the ORR mass activity. However, it is worthwhile to discuss the observed trend in alloying extent and Pt d-band vacancy with respect to the ORR activity, as we believe that it will be more appropriate at this juncture. As mentioned above, the increase in alloying extent observed in the Pt_3Cr_1/C TD catalyst is accompanied with a parallel decrease in its Pt d-band vacancy, as a result of electron donation from Cr to Pt atoms (stronger electronic effect), which could lead to higher electron density around the Pt atoms (d-band filling). This phenomenon should cause an increase in ORR mass activity. On the basis of our results and the facts discussed above, the observed trend in ORR mass activity may be explained as follows. The decrease in the Pt electroactive surface area would tend to decrease the ORR mass activity. On the other hand, an increase in alloying extent and subsequent decrease in Pt d-band vacancy would lead to increased ORR mass activity. The above two effects nullify each other in the Pt_3Cr_1/C NPs, and the observed ORR mass activity should be the result of the two opposite effects, whereby in this case the activity of a catalytic site, that is, alloying extent and Pt d-band vacancy play dominant roles determining the enhanced ORR activity. This finding is in a good agreement with previous studies, where the structural (e.g., lattice parameter, alloying extent) and electronic (i.e., Pt d-band vacancy) effects are of significance in governing the ORR activity. Thus, synthetic approaches that can control the atomic composition of bimetallic NPs with a high alloying extent and convenient electronic structure offer the possibility of achieving promising ORR electrocatalysts.

In the context of the ORR mechanism, we additionally determined the ORR kinetic parameters, that is, the number of electrons transferred during the reaction. This determines whether the catalyst follows the two-electron or direct four-electron pathway of oxygen reduction to water. On the unwanted two-electron pathway, O_2 is reduced first to intermediate hydrogen peroxide, which could harm fuel cell components such as the membrane, and then to water [Eqs. (7) and (8)], but this is averted by the direct pathway, since O_2 is directly reduced to water [Eq. (9)].

$$O_2 + 2\,H^+ + 2\,e^- \rightarrow H_2O_2 \tag{7}$$

$$H_2O_2 + 2\,H^+ + 2\,e^- \rightarrow 2\,H_2O \tag{8}$$

$$O_2 + 4\,H^+ + 4\,e^- \rightarrow 2\,H_2O \tag{9}$$

For this purpose, a significantly reduced catalyst loading $(0.22\,mg_{Pt}^{-1}\,cm^{-2})$ was used to expand the range of experimentally accessible mass-specific current densities to values which are typically obtained in DMFCs, that is, a typical Pt loading of 2–$5\,mg_{Pt}^{-1}\,cm^{-2}$.[3] Under such conditions, the exposed catalyst surface is sufficient to neglect any important diffusion-resistance contribution of the catalyst layer.[46,47]

Therefore, accurate and fast determination of kinetic parameters with respect to ORR in the absence of mass-transport effects could be adjusted to the simple Koutecky–Levich first-order reaction.

In the Koutecky-Levich first-order reaction, the overall current density j is only related to the kinetic current density j_k and the diffusion-limiting current density j_d [Eq. (10)][48–51]

$$\frac{1}{j} = \frac{1}{j_k} + \frac{1}{j_d} \quad (10)$$

where j_d can be expressed as [Eq. (11)].

$$j_d = 0.62 n F D^{2/3} \nu^{-1/6} C \omega^{1/2} = B C \omega^{1/2} \quad (11)$$

in which n is the number of electrons involved in the ORR, F the Faraday constant ($96485\ C\,mol^{-1}$), D the diffusion coefficient of oxygen in the electrolyte ($1.9 \times 10^{-9}\ m^2\,s^{-1}$), ν the kinematic viscosity of the electrolyte ($1.0009 \times 10^{-6}\ m^2\,s^{-1}$), C the concentration of oxygen in the electrolyte ($1.2 \times 10^{-6}\ mol\,m^3$), B the Levich constant, and ω the rotation rate of the electrode.[48,52]

Figure 5a–c shows polarization curves for oxygen reduction at different rotation rates for the Pt/C E-tek and Pt$_3$Cr$_1$/C catalysts. Their current densities are clearly proportional to the applied rotation rate. From these polarization curves, the Koutecky–Levich plots for all catalysts were drawn by using Equations (10) and (11), as shown in in Figure 5d. The plot of j^{-1} versus $\omega^{-1/2}$ yields a straight line, which implies a first-order dependence of O_2 kinetics, as described by Stamenković et al.[53,54] The corresponding slope was then used to determine the Levich constant B, from which the number of electrons transferred can be calculated. Additionally the intercept of the plot can give the reciprocal of the kinetic current density j_k. The Levich constant B calculated from Equation (11) for the 0.5 M H_2SO_4 solution together with its properties (e.g., D, ν, and C) were applied in Equation (12) to calculate the number of transferred electrons n.

$$n = \frac{B}{0.62 F D^{2/3} \nu^{-1/6} C} = \frac{B}{0.02715} \quad (12)$$

The B value for all the catalysts is nearly identical to the theoretical value ($B = 0.1086\ mA\,cm^{-2}\,(rpm)^{-1}$) for $n = 4$,[48] for which oxygen reduction proceeds by transfer of four electrons and thus involvement of intermediate species (i.e., H_2O_2) in the ORR could be averted. Close inspection of Figure 5d reveals that all the catalysts have similar slopes but their intercepts are different, which strongly suggests that all catalysts follow the same reaction pathway (i.e., direct four-electron) and have the same rate-determining step in the ORR but that their kinetic activities for this reaction are different. Both Pt$_3$Cr$_1$/C catalysts show a drastically enhanced kinetic parameter j_k compared to Pt/C E-tek. Moreover, the Pt$_3$Cr$_1$/C TD catalyst, which has a better alloying extent and higher electronic effect than the Pt$_3$Cr$_1$/C EG catalyst, has a larger kinetic parameter j_k. This is again mainly due to the excellent control over the alloy composition of Pt$_3$Cr$_1$/C TD catalyst. It is interesting to point out the viability of the present TD method in achieving precise control over the composition of the bimetallic PtCr NPs with a uniform particle dispersion throughout the entire region of the carbon support; these NPs (size ca. 3–3.5 nm) also showed significantly enhanced ORR activity through a favorable direct four-electron reaction pathway. In the following discussion, we additionally evaluate the selectivity of the Pt$_3$Cr$_1$/C TD catalyst towards the ORR in the presence of methanol. Various concentrations of methanol were introduced into the electrolyte solution such as to mimic the conditions of methanol crossover, and thus the methanol tolerance of the catalyst could be studied.

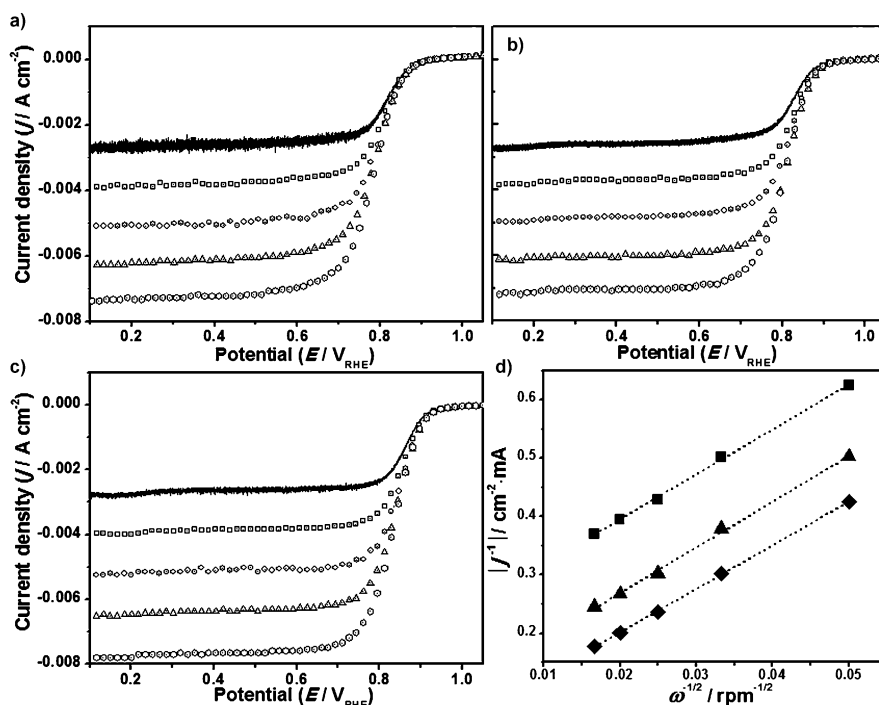It is known that a further reduction of the cell voltage by

Figure 5. Polarization curves at different rotation rates recorded in O_2-saturated 0.5 M H_2SO_4 with a scan rate of $1\ mV\,s^{-1}$ at 25 °C for a) Pt/C E-tek (20 wt %), b) Pt$_3$Cr$_1$/C EG and c) Pt$_3$Cr$_1$/C TD catalysts; ——: 400, □: 900, ◇: 1600, △: 2500, and ○: 3600 rpm. d) Corresponding Koutecky–Levich plots at 0.8 V (RHE); ■: Pt/C E-tek, $j_k = 4.26$, $n \approx 4$; ▲: Pt$_3$Cr$_1$/C EG, $j_k = 11.93$, $n \approx 4$; ◆: Pt$_3$Cr$_1$/C TD, $j_k = 19.23$, $n \approx 4$.

about 200–300 mV is caused by crossover of methanol from the anode to the Pt-based cathode. Methanol oxidation at the cathode not only reduces the cell voltage because of poisoning caused by intermediates produced during methanol dissociation, but is also a waste of fuel, because there is no electron transfer in response to the external load.[18,20,27,55] Thus, it is very important to develop high-performance ORR electrocatalysts which can tolerate the effects of methanol crossover in DMFCs. Figure 6 shows the polarization curves of oxygen reduction at different concentration of methanol for the Pt/C E-tek and Pt_3Cr_1/C catalysts. In the presence of 0.05 M methanol in the working electrolyte, a significant increase in over-potential (ca. 300 mV) for the ORR on Pt/C E-tek catalyst was observed. This is due to competition between oxygen reduction and methanol oxidation. At this junction, a combination of oxygen reduction and methanol oxidation in the overall electro-chemical process leads to formation of mixed potentials. In contrast, both the Pt_3Cr_1/C catalysts show only a small response towards the methanol oxidation reaction (MOR). This result shows that both the Pt_3Cr_1/C catalysts are weakly impacted by the presence of methanol in the electrolyte. Thus, their selectivity to ORR over the MOR is higher than that of the Pt/C catalyst. This can be ascribed to the weakly competitive reaction of methanol oxidation, which could mainly originate from the composition effect (especially the Pt electroactive site) and the disordered alloy structure induced by the presence of Cr atoms,[18,20] as discussed below.

For the methanol oxidation, at least three adjacent Pt sites in the proper spatial arrangement are required in the methanol chemisorptions step. For PtCr alloys with a disordered structure, the probability of finding three neighboring Pt atoms on the surface is lower if no Pt enrichment on the surface takes place. Since dissociative chemisorption of methanol requires at least three adjacent Pt atoms, the presence of methanol-tolerant Cr atoms around the Pt active sites can block methanol adsorption on Pt due to a dilution effect. Consequently, methanol oxidation on these Pt alloy catalysts is suppressed, and this suggests that the MOR is affected predominantly by the surface population of Pt electroactive sites, rather than the structural (alloying extent) and electronic (Pt d-band vacancy) properties of that Pt site.

On the other hand, oxygen adsorption in the ORR, which is usually regarded as being due to dissociative chemisorption, requires only two adjacent Pt sites, whereby the structural and electronic properties of the Pt site play a dominant role and are of significance determining the ORR activity, as was discussed above.

From the above mentioned facts, with increasing Cr content in the disordered PtCr alloys, we expect a higher selectivity with respect to ORR than to MOR. Analysis of the electrochemical active surface area of both disordered-structured Pt_3Cr_1/C catalysts in Table 1 revealed that the Pt_3Cr_1/C catalyst prepared by the present TD method has a higher Cr content, as indicated by its lower number of Pt electroactive sites compared to that prepared by the conventional EG method. This can explain the fact that the Pt_3Cr_1/C TD catalyst is the least impacted by the presence of methanol and thus may lead to enhanced methanol tolerance during the course of ORR. The higher alloying extent and the subsequent increase in its electronic effect together with the higher Cr surface content in Pt_3Cr_1/C TD catalyst mutually act to give enhanced ORR activity with suppressed ORR.

Accelerated stability tests for both Pt_3Cr_1/C catalysts and the Pt/C catalyst were performed under harsh electrochemical treatment in acid media, in which the catalysts were subjected to repetitive potential cycling from 0.05 to 1.10 V for 2000 cycles at a scan rate of 500 mV s^{-1} in 0.5 M sulfuric acid solution. Under these conditions, surface oxidation/reduction reactions of the Pt atoms take place. The surface reaction involves formation of PtOH and PtO derived from oxidation of water, which causes dissolution of Pt via the Pt^{2+} oxidation state. For each 250 cycles, the CV was recorded (see Figure 7 a–c), and from its corresponding anodic currents in the hydrogen adsorption–desorption region, we then calculated the Pt electroactive surface area. As shown in Figure 7 a and b, for both Pt_3Cr_1/C catalysts no marked changes in the shape or size of their CVs are observed during this accelerated stability test, and their Pt electroactive surface area remain unchanged (Figure 7 d). This reveals that both catalysts are highly stable, and thus no significant change in the Pt/Cr ratio occurs. This is the main reason why the ORR activities for both of these Pt_3Cr_1/C catalysts are maintained even after 2000 cycles of severe stability test-
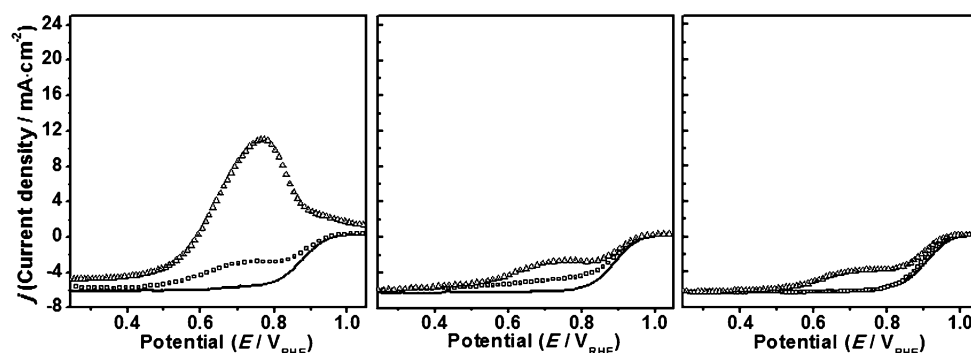

Figure 6. Polarization curves at various concentrations of methanol (20 mL) recorded in O_2-saturated 0.5 M H_2SO_4 with a scan rate of 1 mV s^{-1} at 25 °C for Pt/C E-tek (20 wt %; left) and Pt_3Cr_1/C EG (center) and Pt_3Cr_1/C TD (right) catalysts; ——: without MeOH, □: with 5 mM MeOH, △: with 50 mM MeOH.
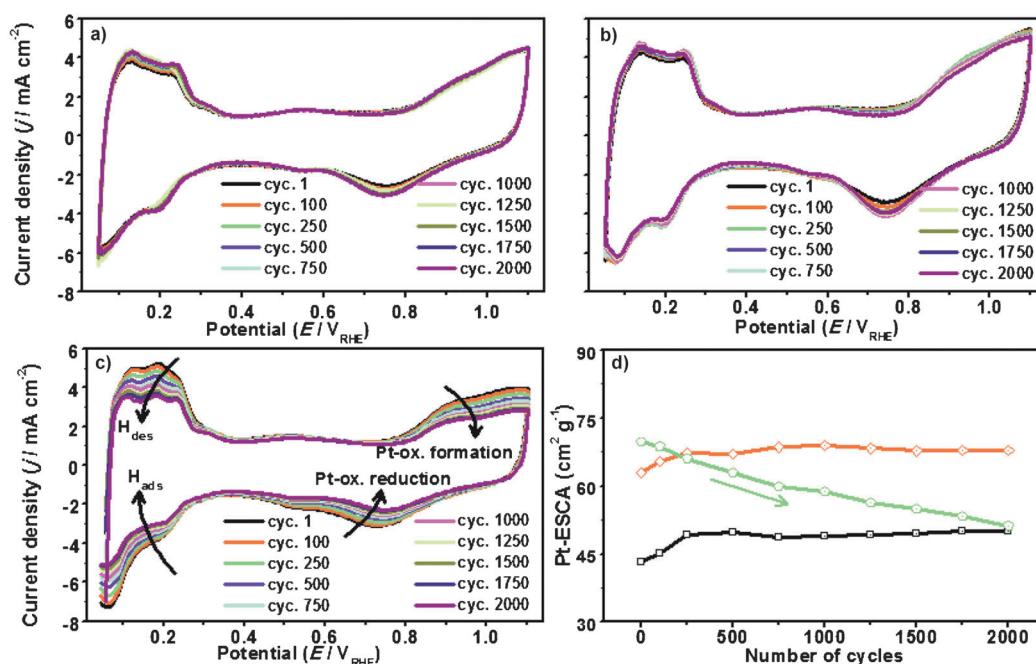
Figure 7. Cyclic voltammograms during repetitive potential cycling in 0.5 M H$_2$SO$_4$ for the Pt$_3$Cr$_1$/C catalysts prepared by a) the TD and b) the EG method and c) for the Pt/C E-tek catalyst (20 wt %). d) Corresponding calculated Pt-electroactive surface area for Pt$_3$Cr$_1$/C TD (black line), Pt$_3$Cr$_1$/C EG (orange line), and Pt/C E-tek (green line).

ing up to 1.10 V (Supporting Information, Figure S6a and b). In contrast, the Pt electroactive surface area of the Pt/C catalyst gradually decreases with increasing number of cycles; it drops from 69.80 to 51.29 cm^{2}g^{-1} after 2000 cycles, which is attributed to at least two closely connected effects:[56] 1) leaching of platinum from the catalyst surface and subsequent Pt deposition (Ostwald ripening), and 2) agglomeration/growth of the Pt particles due to crystallite migration on carbon supports. The extent of these effects on the Pt/C catalyst could also be clearly seen in the changes in its corresponding CV features (Figure 7c), where both the anodic and cathodic currents in hydrogen and metal-oxide regions were significantly suppressed. Consequently, the corresponding ORR polarization curve for this Pt/C catalyst after 2000 cycles was dramatically shifted to lower potential compared to the initial state (Supporting Information, Figure S6c), which means that a significant degradation of ORR activity took place.

The Pt–Cr alloy catalyst has higher stability than other Pt–M alloys used for the ORR, for example, Pt–Cu, Pt–Mn, and Pt–Fe alloys, which are unstable to similar repetitive potential cycling, since the second metal M is leached.[33,57] The free energies of formation, which are an indication of thermodynamic stability, were calculated for various Pt–M alloys, including Pt–Cr, by Glass and Cahen[19] using the Kaufman approach, which is well-known in the areas of phase transformations and thermodynamics. It was found that Pt–Cr alloy has the largest negative free energy of formation. From a thermodynamic standpoint, this finding indicates that these alloys have the largest driving force against alloy decomposition, which can occur in electrochemical en-

vironments. The addition of Cr atoms possibly confers stability by raising the oxidation potential of Pt, which can block the kink and step sites of Pt where dissolution starts.[10] Thus, a greater alloying extent of Pt–Cr alloys is expected to lead to a larger free energy of formation, as the extent of the electronic effect, that is, hybridization between the Cr (3d) and Pt (5d) states is noticeably increased, which may lead to a large free energy of formation. However, although the two Pt$_3$Cr$_1$/C catalysts have different alloying extents, they have similar high stability. This phenomenon can be explained from their equilibrium phase diagram (at 25 °C), which depicts the curve of the free energy formation versus the atomic fraction of Cr. The variation of Cr content from 15.43 (EG catalyst) to 26.22 (TD catalyst) leads to small differences in their free energies of formation, that is, from 10.2 to 14.2 kcal g-atom^{-1}; these values are still considered to give high stability compared to other bimetallic Pt alloys.[19]

Conclusion

Three important parameters in an oxygen reduction reaction, namely the electrocatalytic activity, selectivity and stability, have been simultaneously studied on the basis of different alloying extents (structure) in Pt$_3$Cr$_1$/C nanocatalysts. Starting from the same designed alloy composition, we employed two different methods to prepare Pt$_3$Cr$_1$/C nanocatalysts with different alloying extents. The TD method was developed in this study for preparing a catalyst with well-controlled composition, in which the chemical reduction of Pt

precursor took place at at a rate that matches that of slow thermal decomposition of the organometallic Cr precursor. On the contrary, the ethylene glycol method is unable to control its composition, as a considerable deviation of more than 25 % from the designed composition was observed. Owing to fine control of alloy composition, the Pt_3Cr_1/C catalyst prepared by the TD method has a higher alloying extent than the catalyst prepared by the EG method. Using a combination of XAS, TEM, DFT calculations and electrochemical techniques, we have shown that the alloying extent can affect other physiochemical properties of the Pt_3Cr_1/C alloy catalysts, namely, the Pt d-band vacancy and the Pt ESCA, and is of significance in determining the ORR activity, selectivity, and stability. For the ORR activity, the effects of the alloying extent and the Pt d-band vacancy (electronic effect) are more dominant in compensating the effect of the Pt ESCA. To give selectivity for ORR over the competitive MOR, these effects worked mutually in such a way that the MOR is suppressed while the course of ORR is undisturbed. Addition of Cr atoms within the Pt_3Cr_1/C alloy catalyst stabilizes this catalyst, and prevents particle destruction during electrochemical treatment. Overall, this study emphasizes the significance of controlled-composition synthesis in yielding a favorable alloying extent, Pt d-band vacancy and Pt ESCA, which lead to superior ORR activity, selectivity, and stability, as demonstrated by the Pt_3Cr_1/C TD catalyst.

Experimental Section

Preparation of modified carbon supports: Vulcan XC-72R carbon was modified to obtain desired changes in surface structure. We referred to a method reported by Li et al.[58] and changed it for preparation of the modified Vulcan XC-72R carbon supports. This modified Vulcan XC-72R carbon was used as support for both Pt_3Cr_1/C TD and Pt_3Cr_1/C EG NPs. Combinations of acid reflux with appropriate solvent mixtures were used not only to remove metal impurities, but also generate new oxygen functional groups on the surface of Vulcan XC-72R carbon. Thus, the large number of free reactive sites that were generated from those functional groups facilitates the deposition and dispersion of catalysts on Vulcan XC-72R carbon. The surface of Vulcan XC-72R carbon was modified by treatment with nitric acid solution (65 %) under reflux at 100 °C for 8 h with stirring. After centrifugation at 18 000 rpm, the resulting precipitate was washed several times with water and few drops of ammonia solution (35 %) to give neutral pH. After washing, the Vulcan XC-72R carbon was dried overnight in air in an oven at 80 °C.

Preparation of Pt_3Cr_1/C NPs: Highly dispersed Pt_3Cr_1/C TD NPs with uniform size and tight control of composition were prepared by using a modification of the method proposed by Sun et al.[23] The NPs (metal loading 30 wt %) were prepared by chemical reduction of [Pt(acac)₂] and thermal decomposition of [Cr(CO)₆] on the modified Vulcan XC-72R carbon supports in benzyl ether in with the presence of oleic acid and oleylamine under N₂ atmosphere. In a typical procedure, 1.5 mmol of [Pt(acac)₂] and 0.5 mmol of [Cr(CO)₆] were added to a 100 mL reaction flask containing a magnetic stirring and dissolved in a mixed solvent of benzyl ether (30 mL) and 1,2-hexadecanediol (400 mg). After purging with N₂ for 30 min at room temperature, the reaction flask was heated to 120 °C for 15 min and oleic acid (160 μL), oleylamine (500 μL) and modified Vulcan XC-72R carbon (745 mg) were added. The obtained mixtures were then heated to reflux at 290 °C for 1 h with heating rate of 5 °C min⁻¹ before cooling to room temperature. As reference catalyst, Pt_3Cr_1/C EG NPs were prepared by an EG method,[21] in which PtCl₄,

CrCl₃, EG (as solvent and reducing agent) and modified Vulcan XC-72R carbon support were first mixed, the pH was then adjusted to 11 by adding saturated NaOH in EG solution and finally the mixtures were refluxed at 160 °C for 3 h under N₂ atmosphere. The mixtures from both the methods were cooled to room temperature and washed by centrifugation at 22 000 rpm for 30 min. Ethanol and hexane, respectively, were used to wash and redisperse the particle catalysts, and this was repeated at least five times. After washing, the obtained sample was dried at 80 °C in an air oven for about 8 h. In order to ensure a complete removal of residual organic compounds; all catalysts were subjected to a flowing 10 % H₂ gas at 300 °C for 2 h.

TEM and XAS measurements: TEM studies were performed on a Philips/FEI Tecnai 20G2 S-Twin microscope operated at an accelerating voltage of 200 kV. Specimens were prepared by ultrasonically suspending the nanoparticles in ethanol, applying the suspension to a copper grid and drying in air. The alloy compositions were quantitatively analyzed by TEM coupled with energy-dispersive X-ray analysis (EDX, JEOL JSM-6330F). The XAS spectra were recorded at the Taiwan Beam Line of BL07A1 at the NSRRC, Hsinchu, Taiwan. The electron storage ring of NSRRC was operated at 1.5 GeV. A double Si(111) crystal monochromator was employed for energy selection with a resolution $\Delta E/E$ better than 1×10^{-4} at both the Pt L_3-edge (11564 eV) and Pt L_2-edge (13273 eV). All spectra were recorded at room temperature in transmission mode. Three gas-filled ionization chambers were used in series to measure the intensities of the incident beam I_0, the beam transmitted by the sample I_t and the beam subsequently transmitted by the reference foil I_r. The third ion chamber was used in conjunction with the reference samples, which was a Pt foil for both the Pt L_3- and L_2-edges. The control of parameters for EXAFS measurements, data collection modes and calculation of errors were all done as per the guidelines set by International XAFS Society Standards and Criteria Committee.[59]

Electrode preparation and electrochemical measurements: Millipore water (18 MΩ) and sulfuric acid (Across) were used in this study. All experiments were carried out at ambient temperature of 25 ± 1 °C. A conventional three-electrode electrochemical cell was used for the electrochemical measurements, with a high surface area Pt counter-electrode and a saturated calomel electrode (SCE) reference [all potentials in this paper are quoted versus the reversible hydrogen electrode (RHE)], powered by a Solartron (1480 model) potentiostat/galvanostat. The working electrode was made of the carbon-supported Pt and PtCr catalysts immobilized on glassy carbon electrode (GCE, surface area 0.1964 cm²). The procedure for electrode fabrication involved 1) preparation of a clear suspension by sonicating a known amount of Pt/C and PtCr/C powder dispersed in 0.5 % Nafion; 2) placing an aliquot of the suspension (7 μL of 6.2 μg_Pt mL⁻¹ of the catalyst) on the GCE disc; 3) air-drying for about 5 min at room temperature and then at 80 °C to yield a uniform thin film of the catalyst. 0.5 M sulfuric acid was used as supporting electrolyte for all the experiments. After fabrication the electrodes were immersed in 200 mL of N₂-saturated 0.5 M sulfuric acid, and the potential was scanned from 0.00 to 1.1 V (RHE) for about 10 cycles at a scan rate of 0.05 V s⁻¹ for pretreatment. Then the cyclic voltammetry experiments were performed at a scan rate of 10 mV s⁻¹. The electrochemical performance of the ORR was evaluated by using the combined linear-scan voltammetry (LSV) technique and a rotating-disc electrode (RDE) instrument (Autolab speed control). Prior to the ORR experiments, the same electrolyte solution was purged with O₂ gas for 30 min, and then the hydrodynamic voltammograms for the ORR were recorded by sweeping the potential from 0.05 to 1.10 V at 1 mV s⁻¹. The rotation rates were 400, 900, 1600, 2500 and 3600 rpm.

Acknowledgements

[1] S. Alayoglu, A. U. Nilekar, M. Mavrikakis, B. Eichhorn, *Nat. Mater.* **2008**, *7*, 333–338.

[2] P. Strasser, S. Koh, T. Anniyev, J. Greeley, K. More, C. Yu, Z. Liu, S. Kaya, D. Nordlund, H. Ogasawara, M. F. Toney, A. Nilsson, *Nat. Chem.* **2010**, *2*, 454–460.

[3] J. I. Park, J. Cheon, *J. Am. Chem. Soc.* **2001**, *123*, 5743–5746.

[4] W. R. Lee, M. G. Kim, J. R. Choi, J. I. Park, S. J. Ko, S. J. Oh, J. Cheon, *J. Am. Chem. Soc.* **2005**, *127*, 16090–16097.

[5] S. Zhang, F. J. Lopez, J. K. Hyun, L. J. Lauhon, *Nano Lett.* **2010**, *10*, 4483–4487.

[6] B. J. Hwang, L. S. Sarma, J. M. Chen, C. H. Chen, S. C. Shih, G. R. Wang, D. G. Liu, J. F. Lee, M. T. Tang, *J. Am. Chem. Soc.* **2005**, *127*, 11140–11145.

[7] J. Greeley, J. I. E. L. Stephens, A. S. Bondarenko, T. P. Johansson, H. A. Hansen, T. F. Jaramillo, J. Rossmeisl, I. Chorkendorff, J. K. Nørskov, *Nat. Chem.* **2009**, *1*, 552–556.

[8] K. E. Elkins, T. S. Vedantam, J. P. Liu, H. Zeng, S. Sun, Y. Ding, Z. L. Wang, *Nano Lett.* **2003**, *3*, 1647–1649.

[9] M. Chen, J. P. Liu, S. J. Sun, *J. Am. Chem. Soc.* **2004**, *126*, 8394–8395.

[10] J. Zhang, K. Sasaki, E. Sutter, R. R. Adzic, *Science* **2007**, *315*, 220–222.

[11] H. Zhao, B. E. Koel, *J. Phys. Chem. C* **2009**, *113*, 18152–18162.

[12] L. S. Sarma, F. Taufany, B. J. Hwang in *Electrocatalyst Characterization and Activity Validation—Fundamentals and Methods* (Eds.: H. Liu, J. Zhang), Wiley-VCH, Weinheim, **2009**, pp. 115–163.

[13] B. J. Hwang, S. M. S. Kumar, C. H. Chen, Monalisa, M. Y. Cheng, D. G. Liu, J. F. Lee, *J. Phys. Chem. C* **2007**, *111*, 15267–15276.

[14] E. Antolini, *Mater. Chem. Phys.* **2003**, *78*, 563–573.

[15] R. Ferrando, J. Jellinek, R. L. Johnston, *Chem. Rev.* **2008**, *108*, 845–910.

[16] Z. Liu, E. T. Ada, M. Shamsuzzoha, G. B. Thompson, D. E. Nikles, *Chem. Mater.* **2006**, *18*, 4946–4951.

[17] S. Mukerjee, S. Srinivasan, M. P. Soriaga, J. McBreen, *J. Electrochem. Soc.* **1995**, *142*, 1409–1422.

[18] H. Yang, N. Alonso-Vante, J. M. Léger, C. Lamy, *J. Phys. Chem. B* **2004**, *108*, 1938–1947.

[19] J. T. Glass, J. G. L. Cahen, *J. Electrochem. Soc.* **1988**, *135*, 1650–1658.

[20] H. Yang, N. Alonso-Vante, C. Lamy, D. L. Akins, *J. Electrochem. Soc.* **2005**, *152*, A704–A709.

[21] C. Bock, C. Paquet, M. Couillard, G. A. Botton, B. R. MacDougall, *J. Am. Chem. Soc.* **2004**, *126*, 8028–8037.

[22] H. Yano, M. Kataoka, H. Yamashita, H. Uchida, M. Watanabe, *Langmuir* **2007**, *23*, 6438–6445.

[23] S. Sun, C. B. Murray, D. Weller, L. Folks, A. Moser, *Science* **2000**, *287*, 1989–1992.

[24] S. Sun, S. Anders, T. Thomson, J. E. E. Baglin, M. F. Toney, H. F. Hamann, C. B. Murray, B. D. Terris, *J. Phys. Chem. B* **2003**, *107*, 5419–5425.

[25] W. Chen, J. Kim, S. Sun, S. Chen, *Langmuir* **2007**, *23*, 11303–11310.

[26] D. B. Williams, C. B. Carter in *Transmission Electron Microscopy: A Textbook for Material Science* Plenum Press, New York, **1996**.

[27] E. Antolini, J. R. C. Salgado, L. G. R. A. Santos, G. Garcia, E. A. Ticianelli, E. Pastor, E. R. Gonzalez, *J. Appl. Electrochem.* **2006**, *36*, 355–362.

[28] W. B. Pearson in *A Handbook of Lattice Spacings and Structures of Metals and Alloys*, 3rd ed., Pergamon Press, New York, **1964**.

[29] J. R. C. Salgado, E. Antolini, E. R. Gonzalez, *J. Phys. Chem. B* **2004**, *108*, 17767–17774.

[30] C. H. Chen, L. S. Sarma, J. M. Chen, S. C. Shih, G. R. Wang, D. G. Liu, M. T. Tang, J. F. Lee, B. J. Hwang, *ACS Nano* **2007**, *1*, 114–125.

[31] D. Y. Wang, C. H. Chen, H. C. Yen, Y. L. Lin, P. Y. Huang, B. J. Hwang, C. C. Chen, *J. Am. Chem. Soc.* **2007**, *129*, 1538–1540.

[32] B. J. Hwang, L. S. Sarma, G. R. Wang, C. H. Chen, D. G. Liu, H. S. Sheu, J. F. Lee, *Chem. Eur. J.* **2007**, *13*, 6255–6264.

[33] F. J. Lai, W. N. Su, L. S. Sarma, D. G. Liu, C. A. Hsieh, J. F. Lee, B. J. Hwang, *Chem. Eur. J.* **2010**, *16*, 4602–4611.

[34] S. H. Chang, W. N. Su, M. H. Yeh, C. J. Pan, K. L. Yu, D. G. Liu, J. F. Lee, B. J. Hwang, *Chem. Eur. J.* **2010**, *16*, 11064–11071.

[35] A. N. Mansour, J. W. Cook, D. E. Sayers, *J. Phys. Chem.* **1984**, *88*, 2330–2334.

[36] S. N. Reifsnyder, M. M. Otten, D. E. Sayers, H. H. Lamb, *J. Phys. Chem. B* **1997**, *101*, 4972–4977.

[37] J. M. Ramallo-López, G. F. Santori, L. Giovanetti, M. L. Casella, O. A. Ferretti, F. H. Requejo, *J. Phys. Chem. B* **2003**, *107*, 11441–11451.

[38] A. L. Ankudinov, A. I. Nesvizhskii, J. J. Rehr, *J. Synchrotron Radiat.* **2001**, *8*, 92–95.

[39] V. Stamenkovic, B. S. Mun, K. J. J. Mayrhofer, P. N. Ross, N. M. Markovic, J. Rossmeisl, J. Greeley, J. K. Nørskov, *Angew. Chem.* **2006**, *118*, 2963–2967; *Angew. Chem. Int. Ed.* **2006**, *45*, 2897–2901.

[40] A. Pozio, M. De Francesco, A. Cemmi, F. Cardellini, L. Giorgi, *J. Power Sources* **2002**, *105*, 13–19.

[41] V. Jalan, E. J. Taylor, *J. Electrochem. Soc.* **1983**, *130*, 2299–2302.

[42] R. C. Koffi, C. Coutanceau, E. Garnier, J. M. Léger, C. Lamy, *Electrochim. Acta* **2005**, *50*, 4117–4127.

[43] H. Ye, J. A. Crooks, R. M. Crooks, *Langmuir* **2007**, *23*, 11901–11906.

[44] H. Yano, J. Inukai, H. Uchida, M. Watanabe, P. K. Babu, T. Kobayashi, J. H. Chung, E. Oldfield, A. Wieckowski, *Phys. Chem. Chem. Phys.* **2006**, *8*, 4932–4939.

[45] K. J. J. Mayrhofer, B. B. Blizanac, M. Arenz, V. R. Stamenkovic, P. N. Ross, N. M. Markovic, *J. Phys. Chem. B* **2005**, *109*, 14433–14440.

[46] U. A. Paulus, T. J. Schmidt, H. A. Gasteiger, R. J. Behm, *J. Electroanal. Chem.* **2001**, *495*, 134–145.

[47] U. A. Paulus, A. Wokaun, G. G. Scherer, T. J. Schmidt, V. Stamenkovic, N. M. Markovic, P. N. Ross, *Electrochim. Acta* **2002**, *47*, 3787–3798.

[48] F. Dundar, A. Smirnova, X. Dong, A. Ata, N. Sammes, *J. Fuel Cell Sci. Technol.* **2006**, *3*, 428–433.

[49] E. Higuchi, H. Uchida, M. Watanabe, *J. Electroanal. Chem.* **2005**, *583*, 69–76.

[50] N. Hoshi, M. Nakamura, S. Kondo, *Electrochem. Commun.* **2009**, *11*, 2282–2284.

[51] M. H. Shao, T. Huang, P. Liu, J. Zhang, K. Sasaki, M. B. Vukmirovic, R. R. Adzic, *Langmuir* **2006**, *22*, 10409–10415.

[52] C. Jeyabharathi, P. Venkateshkumar, J. Mathiyarasu, K. L. N. Phani, *Electrochim. Acta* **2008**, *54*, 448–454.

[53] V. Stamenković, T. J. Schmidt, P. N. Ross, N. M. Marković, *J. Phys. Chem. B* **2002**, *106*, 11970–11979.

[54] V. Stamenković, T. J. Schmidt, P. N. Ross, N. M. Marković, *J. Electroanal. Chem.* **2003**, *554–555*, 191–199.

[55] Y. Gong, Y. D. Yeboah, S. N. Lvov, V. Balashov, Z. Wang, *J. Electrochem. Soc.* **2007**, *154*, B560-B565.

[56] M. Inaba in *Durability of Electrocatalysts in Polymer Electrolyte Fuel Cells, Vol. 25* (Eds.: T. Fuller, C. Hartnig, V. Ramani, H. Uchida, H. Gasteiger, S. Cleghorn, P. Strasser, T. Zawodzinski, D. Jones, P. Shirvanian, T. Jarvi, P. Zelenay, C. Lamy, P. Bele), ECS Transactions, New Jersey, **2009**, pp. 573–581.

[57] S. Koh, P. Strasser, *J. Am. Chem. Soc.* **2007**, *129*, 12624–12625.

[58] X. Li, Z. Zhu, J. Chen, R. De Marco, A. Dicks, J. Bradley, G. Lu, *J. Power Sources* **2009**, *186*, 1–9.

[59] EXAFS measurement and controlled parameters: a) Guidelines for data collection modes for EXAFS measurements and user-controlled parameters: http://ixs.iit.edu/subcommittee_reports/sc/sc00 report.pdf; b) Guidelines for errors reporting: http://ixs.iit.edu/subcommittee_reports/sc/err.